

An approach to ground based space surveillance of geostationary on-orbit servicing operations



Robert (Lauchie) Scott^a, Alex Ellery^b

^a Defence R&D Canada, 3701 Carling Ave, Ottawa, Ontario, Canada K1A 0Z4

^b Carleton University, Department of Aerospace and Mechanical Engineering, Ottawa, Ontario, Canada

ARTICLE INFO

Article history:

Received 5 November 2014

Received in revised form

5 February 2015

Accepted 7 March 2015

Available online 18 March 2015

Keywords:

Satellite tracking

Space surveillance

Space situational awareness

On-orbit servicing

Differential angles tracking

ABSTRACT

On Orbit Servicing (OOS) is a class of dual-use robotic space missions that could potentially extend the life of orbiting satellites by fuel replenishment, repair, inspection, orbital maintenance or satellite repurposing, and possibly reduce the rate of space debris generation. OOS performed in geostationary orbit poses a unique challenge for the optical space surveillance community. Both satellites would be performing proximity operations in tight formation flight with separations less than 500 m making atmospheric seeing (turbulence) a challenge to resolving a geostationary satellite pair when viewed from the ground. The two objects would appear merged in an image as the resolving power of the telescope and detector, coupled with atmospheric seeing, limits the ability to resolve the two objects. This poses an issue for obtaining orbital data for conjunction flight safety or, in matters pertaining to space security, inferring the intent and trajectory of an unexpected object perched very close to one's satellite asset on orbit. In order to overcome this problem speckle interferometry using a cross spectrum approach is examined as a means to optically resolve the client and servicer's relative positions to enable a means to perform relative orbit determination of the two spacecraft. This paper explores cases where client and servicing satellites are in unforced relative motion flight and examines the observability of the objects. Tools are described that exploit cross-spectrum speckle interferometry to (1) determine the presence of a secondary in the vicinity of the client satellite and (2) estimate the servicing satellite's motion relative to the client. Experimental observations performed with the Mont Mégantic 1.6 m telescope on co-located geostationary satellites (acting as OOS proxy objects) are described. Apparent angular separations between Anik G1 and Anik F1R from 5 to 1 arcsec were observed as the two satellites appeared to graze one another. Data reduction using differential angular measurements derived from speckle images collected by the 1.6 m telescope produced relative orbit estimates with better than 90 m accuracy in the cross-track and in-track directions but exhibited highly variable behavior in the radial component from 50 to 1800 m. Simulations of synthetic tracking data indicated that the radial component requires approximately six hours of tracking data for an Extended Kalman Filter to converge on a relative orbit estimate with less than 100 m overall uncertainty. The cross-spectrum approach takes advantage of the Fast Fourier Transform (FFT) permitting near real-time estimation of the relative orbit of the two satellites. This also enables the use of relatively larger detector arrays ($> 10^6$ pixels) helping to ease acquisition process to acquire optical angular data.

Crown Copyright © 2015 Published by Elsevier Ltd. on behalf of IAA. This is an open access article under the CC BY-NC-ND license (<http://creativecommons.org/licenses/by-nc-nd/4.0/>).

E-mail addresses: robert.scott@drdc-rddc.gc.ca (R. Scott), aellery@carleton.ca (A. Ellery).

<http://dx.doi.org/10.1016/j.actaastro.2015.03.010>

0094-5765/Crown Copyright © 2015 Published by Elsevier Ltd. on behalf of IAA. This is an open access article under the CC BY-NC-ND license (<http://creativecommons.org/licenses/by-nc-nd/4.0/>).

1. Introduction

On Orbit Servicing (OOS) is the on-orbit delivery of interventional services to spacecraft. On Orbit Servicing encompasses a broad area of mission types including satellite rendezvous, inspection, captivation, repair, consumables replenishment (such as fuel or cryogenes), orbital adjustment/deorbit and possibly the on-orbit construction of or reuse of large, complex space structures.

On Orbit Servicing has historically been performed by the manned spaceflight community on Space Shuttle [1], and International Space Station programs [2]. Subsequently, autonomous systems have recently begun to show technical viability in this space mission class. The Japanese ETS-VII mission [3] demonstrated tele-robotic captivation of a small capture article in 1997. The XSS-series [4] of small satellite missions demonstrated autonomous formation flight with an aim to test servicing technologies. Robotic satellite refueling experiments aboard the International Space Station (ISS) [5] are currently being performed with a view toward testing procedures needed for robotic servicing of satellites in geostationary orbit.

The success of the Orbital Express technology demonstration [6] (2007) exemplified the viability of autonomous, robotic, satellite to satellite OOS. Several key space-based mission milestones were achieved without operator intervention including autonomous rendezvous and captivation, hydrazine refueling, battery and electronics replacement.

Subsequent to the Orbital Express mission some industrial proposals [7,8] for geostationary satellite refueling were socialized but were not fully financed. The current DARPA Phoenix [9] mission intends to demonstrate derelict satellite re-use by severing antenna dishes from a geosynchronous satellite and affixing them to a smaller electronics package. This is a complex and challenging orbital construction activity.

While autonomous OOS space missions are yet to be routinely flown it appears that technical maturity has been achieved by several nations and makes it likely that this capability will be fielded in the near future. A future capability to remotely observe OOS activities prior to an object's captivation would be of value to the space surveillance community.

1.1. The space surveillance problem and OOS

While OOS space mission types are yet to become a regular part of the space mission activity, the Space Situational Awareness (SSA) community may be impacted in its ability to track and detect OOS activities occurring in deep space (e.g. geostationary orbit). Space surveillance of deep space orbits (such as geosynchronous orbit) is usually performed with sensitive, wide field, visible-light optical telescopes designed to collect angular measurements and later invoke an orbit determination process to update the orbital catalog. In order to detect small, faint objects in deep space, wide-field images collect large swathes of sky in a single frame collecting both resident space object and background stars. Relatively large pixel scales ($\sim 2\text{--}\sim 6$ arcsec) are used to increase the probability of detection of

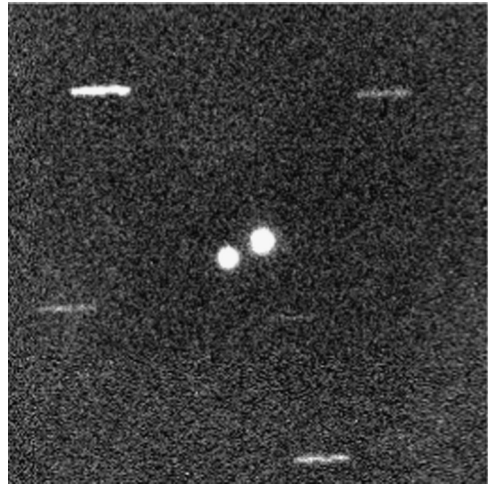


Fig. 1. Satellites (point sources) Anik F1 (lower left) and Anik F1R with background stars. Image credit: DRDC Ottawa Research Center.

an Earth orbiting object and background stars to enable astrometric position measurement. (See Fig. 1).

This approach works well for deep space objects as long as the objects have angular separations larger than a few arcminutes. The typical apparent angular separation between objects in geostationary orbit is $\sim 0.1^\circ$ which is the typical longitude slot width assigned to operational geostationary satellites. Some geostationary operators periodically locate two or more satellites within one slot which tends to force satellites to have angular separations less than 0.05° or less (geostationary satellite co-location). The apparent angular separation is dependent on observer location [10].

An OOS mission would be unobservable to these space surveillance systems as they would be unable to resolve the OOS satellite pairs as their separations are an order of magnitude less than typical in geostationary orbit. The relative distance between the two objects in OOS proximity flight is generally less than 500 m (~ 2.5 arcsec as observed from Earth's surface). Some key impediments prevent OOS activities from being detected; (1) the inherent point spread function of the optics and pixel pitch of the detector array of the telescope and (2) the seeing (turbulence) of Earth's atmosphere. Detectors are only able to resolve the angular information proportional to the size of the pixels and the aperture diameter of telescope, however this can be addressed via good engineering and design. The turbulence-induced "seeing" of Earth's atmosphere is approximately $1\text{--}2$ arcsec (at good astronomical sites) which masks activity which one wishes to observe. At geostationary satellite slant ranges atmospheric seeing scintillates a satellite pair with an effective size of approximately 200–400 m linear distance. If two satellites performing OOS operations are in relative motion closer than the angular size of the atmospheric seeing disk, the atmosphere blurs the position of the satellites together as viewed by the observer (Fig. 2).

OOS missions in geostationary orbit could create new operational issues for SSA operators when the OOS pair have separations less than 500 m. Close proximity

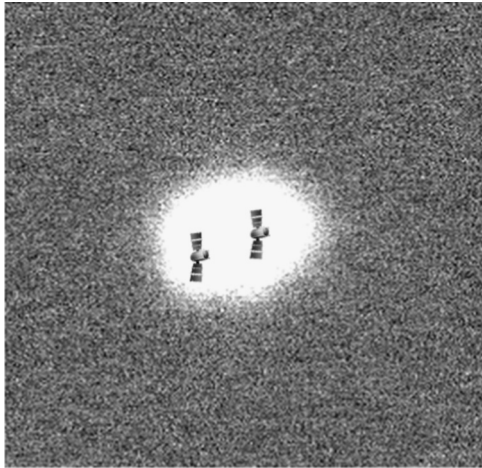


Fig. 2. The On-Orbit Servicing space surveillance problem. Close proximity flight during OOS is masked by the seeing disk of earth's atmosphere when observed from the ground.

formation flight inherently poses an increased risk of satellite collision. Satellite collision warnings, as a matter of general practice, often use orbital measurements independent of satellite operators' positioning data. An independent capability to measure the relative motion between close proximity OOS satellites adds an additional verification mechanism for "cooperative" OOS flight safety where the servicer's intervention is desired and expected. With regard to space security an ability to infer the intent of an unexpected, unknown or uncooperative object in very close proximity to one's own satellite asset would also be of value. Analysis of the relative orbit of the unknown object can establish if the object is a slowly-separating piece of debris, is performing a simple fly-by, is performing complex fly-around inspection maneuvers, or perching in-track from the satellite asset.

Radar systems which offer all-weather observation, could perform differential ranging measurements on an OOS satellite pair and not suffer the same atmospheric degradation as an optical telescope. However, radars have large power requirements in order to detect objects in geostationary orbit. Expense, coupled with the relative scarcity of such powerful radars globally, makes their use constrained by availability.

Optical systems could overcome the limitations of atmospheric seeing by use of Adaptive Optics (AO) and deconvolution techniques in order to obtain diffraction limited imagery. This is difficult to achieve during observation of satellites as guide stars (usually required for AO systems) move relative to the satellite. Laser guide stars can be incorporated but add additional system expense and complexity. The computational expense that deconvolution incurs does not lend itself well to real time measurement.

An alternative means to achieve diffraction limited resolution of an atmospherically blurred astronomical scene exists. Speckle interferometric techniques used by the binary star astronomical community can be used to reconstruct the separation distance and orientation of two objects in the face of random, blurred atmospheric

distortion. This approach, while limited to night-time observation under clear skies, can be adapted at relatively lower expense at a variety of telescopes globally for OOS observation and take advantage of computationally efficient algorithms (such as the FFT). In addition, telescopes in small (< 1 m) and medium (1–3 m) classes are relatively abundant in comparison to radars making sensor availability easier to achieve.

The goal of this research is to achieve subarcsecond (< 200 m at geostationary ranges) relative positional knowledge of uncaptured OOS satellites such that relative orbits in geostationary orbit can be estimated. This study examines a re-imagining of single aperture cross spectrum speckle interferometry as a means to measure relative orbit position data on geostationary satellites performing OOS. Adapting a speckle interferometric approach offers a capability to perform tracking on closely spaced objects far from the Earth while simultaneously offering a workable image processing approach leading to near-real time relative orbital estimates. An observational approach is devised in this paper and framework is established to help answer some key SSA questions regarding OOS flight in geostationary orbit, such as: (1) is there something in very close proximity to my satellite? (2) where is it? and (3) what is its motion?

Differential angular measurements have been examined as a means to measure the relative motion of well separated (several arcminutes or more) co-located geostationary satellites [11,12]. However, this approach relied on both satellites cooperatively radio beaconing a ground station. This type of cooperation cannot be expected in the general SSA surveillance context as the client and/or servicer may not be transmitting complimentary positional information. Optical differential angular astrometry has been successfully used on moving planetary bodies. Knox [13] used speckle interferometry to measure precise relative astrometric positions on moving celestial objects where Pluto nearly occulted a background star. Knox's approach used a linear model of planetary motion but achieved remarkable astrometric precision (0.003 arcsec) in the determination of the distance which Pluto missed the occulting star.

This study combines the principles of differential angular measurements of relative satellite motion with a modified speckle interferometric approach to yield a potential means to monitor OOS operations in geostationary orbit. Findings from experimental measurements collected on two co-located geostationary satellites which performed a close "optical conjunction"¹, a condition where two geostationary satellites appear to encounter one another but are radially separated by 10 km or more, are shown in Section 7. Speckle measurements collected during the encounter serve to help validate the speckle approach as a means to address the problem of OOS space surveillance.

¹ The term "optical conjunction" instead of "visual conjunction" is used in this manuscript to more accurately reflect the line of sight nature of two satellites appearing to coincide on the sky.

2. Observational convention

In this paper the convention used to refer to the “client” (also known as the “primary”) and “servicer” (also referred to as the “secondary”) adheres to the brightness convention used by the astronomical binary star community. The “primary” star is identified as the brighter of the two stars in a binary pair. As applied to OOS satellites the brighter object is considered to be the “client” (“primary”) satellite and the fainter object is considered to be the “servicer” (the “secondary”).

3. Speckle interferometry

The resolving power of a telescope is inversely proportional to the aperture diameter of the telescope. In the visible band, the Rayleigh limit of an optical telescope can be estimated by:

$$\theta = \frac{0.14}{D} \quad (1)$$

where D is in meters and θ is in arcseconds. For 1 m and 10 cm telescopes the Rayleigh limits are approximately 0.14 and 1.4 arcsec respectively.

Earth’s atmosphere however, rarely affords “seeing” conditions matching the diffraction limit of a telescope. In general, atmospheric turbulence induces a perceived 1–3 arcsec of blurring and can limit data from both large and small telescopes to the size of the seeing disk of the atmosphere. Despite the increased sensitivity and expense of a 1 m telescope it is effectively degraded to a resolving capability less than that of a 10 cm telescope due to atmospheric seeing.

This problem has been known for some time and adaptive optics, space based telescopes and image processing techniques can address this problem but are significantly complex and capitially intensive. The binary star astronomy community, which attempts to measure the orbit of stars gravitationally bound to each other, devised an economical and elegant means to extract the key information of the orientation and separation between two objects within the seeing disk. Antoine Labeyrie devised a method [14] to measure the separation and orientation angles of closely spaced double stars by using averaged Fourier transforms of multiple short exposure (5–10ms) images of stars (see Fig. 3 left). The short exposures freeze the instantaneous turbulence effects of the atmosphere over seeing cells of the same size (isoplanatic condition). Labeyrie’s technique is based on measuring the orientation angle and separation of interference fringes which occur in the Fourier plane (refer to Fig. 3) and enables diffraction limited measurement of two stars without needing to reconstruct an image.

The Fourier transform is sensitive to repeating patterns formed during speckle imaging the stacking and averaging of the complex Fourier data preserves the key information required from the atmospherically blurred image. The fringe direction is perpendicular to the separation of the two objects and the spacing between the fringes is inversely proportional to the objects’ separation.

Despite the elegance of this approach, a 180° direction ambiguity occurs in the orientation angle due to the functional symmetry of the Fourier transform. The direction of the fainter object relative to the brighter object is not directly measureable and both orientations will result in a fringe pattern such as that seen in Fig. 3 (right).

Bagnuolo [15] adapted the image autocorrelation (a Fourier complement of the modulus of the Fourier transformed image) to directly highlight the true position of the secondary component. The autocorrelation of an image is calculated as:

$$|I(x,y)|^2 = \sum_{k=0}^{M-1} \sum_{j=0}^{N-1} i(x,y)i(x-k,y-j) \quad (2)$$

where i is the image, N and M are the image size and k and j are the autocorrelation shift delays applied to the imaging plane. Bagnuolo imposes a condition on the autocorrelation where the interior product in Eq. (2) is set to zero if the following condition is met

$$\begin{aligned} i(x,y)i(x-k,y-j) &= 0 \\ \text{if } i(x-k,y-j) &> i(x,y) \end{aligned} \quad (3)$$

This adjustment biases the position of the true location of the secondary over the ambiguity and is called the Directed Vector Autocorrelation (DVA). It produces an approximate image of the binary pair with a suppressed ambiguity star and highlighted secondary.

While DVA works well for binary star observation, it is not well suited for space surveillance if the size of the images to be processed is much larger than 64×64 pixels. The four embedded loops implied by Eq. (2) results in long processing delays even on many modern microcomputers.

Another approach was investigated (and later adopted) in the search for a speckle algorithm to detect closely spaced satellites through atmospheric turbulence. Aristidi [16] invoked another means in which to observe binary stars and resolve the ambiguity issue. The cross correlation of an image (shown in one dimension here for simplicity) is computed as:

$$K_O(\rho) = \int_{-\infty}^{\infty} O^2(x)O(x+\rho)dx \quad (4)$$

where $O(x)$ is the speckle image and ρ is the lag shift on the image. The cross correlation can be efficiently computed by implementing

$$K_O(u) = \left\langle \mathfrak{F} \left[\hat{I}^2 \right] \mathfrak{F} \left[\hat{I} \right]^* \right\rangle \quad (5)$$

where \mathfrak{F} denotes the two dimensional Fourier transform of the zero-mean image I and $\langle \rangle$ brackets denotes the ensemble average of a stack of speckle images.

The cross spectrum (the Fourier transform of the cross correlation) contains real and imaginary parts which fully contains the information required in order to estimate the separation and orientation of a binary star pair. In one dimension, the cross spectrum’s complex components [16] are resolved in the following equations:

$$\text{Re}[K_O(u)] = 1 + \alpha^3 + \alpha(1 + \alpha) \cos(2\pi u d) \quad (6)$$

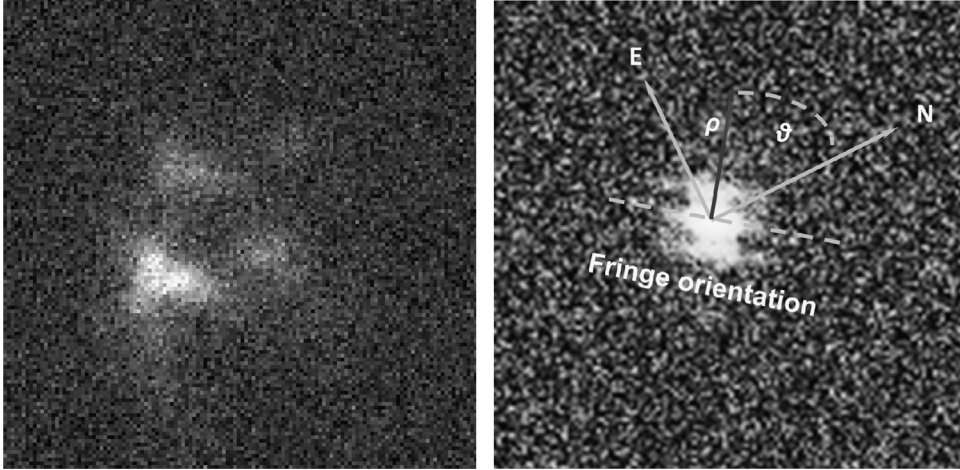


Fig. 3. Left: speckle image of binary star pair Struve 174. Right: modulus of Fourier transform of the speckle images with fringe orientation angle and celestial North references indicated. The ρ vector indicates the direction of the secondary star and is perpendicular to the fringe angle.

$$\text{Im}[K_O(u)] = \alpha(1 - \alpha) \sin(2\pi ud) \quad (7)$$

In Eqs. (6) and (7) α is the ratio of brightness of the two objects, d is the linear separation of the two objects and u is the spatial frequency of the image. By examining the slope of the imaginary part of the cross correlation data at the origin, the direction of the brighter object can be directly ascertained by evaluating

$$\text{slope} = \left[\frac{d}{du} \text{Im}[\hat{K}_O] \right]_{u=0} = 2\pi d\alpha(1 - \alpha) \quad (8)$$

The slope of the imaginary component of the fringe profile is negative if $\alpha \leq 1$ and positive if $\alpha \geq 1$. For the examination of the speckle data collected, the slope of the fringe profile at $u=0$ contains all the information describing the direction which points toward the fainter of the two satellites.

Measurement of the relative angle of the cross correlation fringes and their linear separation provides a means to determine the distance ρ and orientation angle θ between the two objects. A pair of measurements (ρ, θ) can be formed as a direct measurement of the separation of the two objects (see Fig. 4). These measurements are commonly used in the binary star community to estimate the orbit of binary star pairs. In this work these measurements are reckoned relative to the *True of Date (TOD)* equator and equinox of the time of measurement. The separation ρ is usually expressed in arcseconds and θ is expressed in degrees.

4. Relative motion dynamics

Closely spaced geostationary satellites are in circular orbits with very small eccentricities making their relative motion well described by the Clohessy Wiltshire [17] equations of motion (also known as Hill's equations [18]).

For two objects in close orbital proximity in a near circular orbit, the radial, in-track and cross track motion of the secondary satellite, relative to the nominal (client)

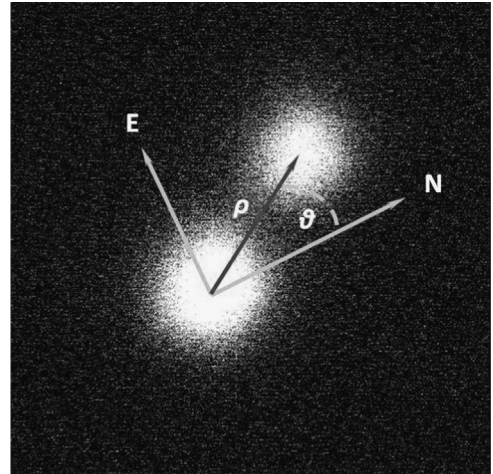


Fig. 4. Definitions of binary star measurements (ρ, θ) relative to the North and East celestial axes.

position is described by The following equation:

$$\begin{bmatrix} \ddot{x} \\ \ddot{y} \\ \ddot{z} \end{bmatrix} = \begin{bmatrix} 2\omega\dot{y} + 3\omega^2x \\ -2\omega\dot{x} \\ -\omega^2z \end{bmatrix} + \begin{bmatrix} A_x \\ A_y \\ A_z \end{bmatrix} \quad \omega = \sqrt{\frac{\mu}{a^3}} \quad (9)$$

where x, y, z are the radial, in-track and cross-track positions of the servicer relative to the client and their velocities and accelerations are denoted with Newton dot notation. Disturbing accelerations (A) such as thrust or solar radiation pressure can be accommodated by integrating the above equations of motion. The mean motion of a geostationary satellite is $\omega = 7.29 \times 10^{-5} \text{ rad s}^{-1}$.

Eq. (9) is a simplified model of satellite formation flight where orbital perturbations resulting from Earth gravitational oblateness, solar radiation pressure, third-body accelerations and satellite thrusting thrust are ignored. A closed form solution to Eq. (9) is expressed in Eq. (10)

which relates the current state at time t to the initial state of the servicer $\mathbf{X}_0 = [\mathbf{x}_0, \mathbf{y}_0, \mathbf{z}_0, \mathbf{v}_{x0}, \mathbf{v}_{y0}, \mathbf{v}_{z0}]^T$.

$$\begin{bmatrix} x(t) \\ y(t) \\ z(t) \\ \dot{x}(t) \\ \dot{y}(t) \\ \dot{z}(t) \end{bmatrix} = \begin{bmatrix} 4-3 \cos(\omega_{\oplus} t) & 0 & 0 & \frac{1}{\omega_{\oplus}} \sin(\omega_{\oplus} t) & \frac{2}{\omega_{\oplus}}(1-\cos(\omega t)) & 0 \\ 6(1-\cos(\omega_{\oplus} t)) & 1 & 0 & \frac{2}{\omega_{\oplus}}(\cos(\omega_{\oplus} t)-1) & \frac{4}{\omega_{\oplus}}(\sin(\omega_{\oplus} t)-3t) & 0 \\ 0 & 0 & \cos(\omega_{\oplus} t) & 0 & 0 & \frac{1}{\omega_{\oplus}} \sin(\omega_{\oplus} t) \\ 3\omega_{\oplus} \sin(\omega_{\oplus} t) & 0 & 0 & \cos(\omega_{\oplus} t) & 2 \sin(\omega_{\oplus} t) & 0 \\ 6\omega_{\oplus}(\cos(\omega_{\oplus} t)-1) & 0 & 0 & -2 \sin(\omega_{\oplus} t) & 4 \cos(\omega_{\oplus} t)-3 & 0 \\ 0 & 0 & -\omega_{\oplus} \sin(\omega_{\oplus} t) & 0 & 0 & \cos(\omega_{\oplus} t) \end{bmatrix} \begin{bmatrix} x_0 \\ y_0 \\ z_0 \\ \dot{x}_0 \\ \dot{y}_0 \\ \dot{z}_0 \end{bmatrix} \quad (10)$$

A state space representation can be written by expressing

$$\vec{\mathbf{x}}(t) = \Phi(t, t_0)\vec{\mathbf{x}}(t_0) \quad (11)$$

where (t, t_0) are current time and epoch times respectively and Φ is the 6×6 state transition matrix from the interior of Eq. (10). Perturbation forces are neglected in this simplified model. The servicer's dynamics adhere to the linearized state space dynamics relationship

$$\dot{\mathbf{x}} = \mathbf{A}\mathbf{x} \quad (12)$$

5. Observation model

Speckle imaging observations (ρ, θ) must be transformed into astrodynamics measurables describing the motion of the satellite pair about one another. The observational geometry where a distant observer collects observations on the combined client+servicer pair is shown in Fig. 5.

Observational coordinates are formed by using vectors describing the position of the geostationary satellites in Fig. 5 and are referenced to the TOD frame. The telescope mount, which has its axes aligned with true celestial north, adheres to the TOD system which simplifies the transform of observation data to the Hill frame due to the use of star trail drifting (see Section 7.1). Geostationary satellite flight is largely along the true equator of date making the TOD frame well matched to satellite orbital motion and the measurables from the telescope. The

position of the servicing satellite relative to the client is expressed as:

$$\mathbf{r}_2 - \mathbf{r}_1 = \vec{\rho}_2 - \vec{\rho}_1 = \Delta \vec{\mathbf{r}} \quad (13)$$

where $\Delta \vec{\mathbf{r}}$ is the position of the servicer with respect to the client. The geocentric position vector $\vec{\mathbf{r}}$ of the satellites in geocentric coordinates is expressed as:

$$\vec{\mathbf{r}} = \begin{bmatrix} r_x \\ r_y \\ r_z \end{bmatrix} = \begin{bmatrix} r_{GEO} \cos(\delta) \cos(\alpha) \\ r_{GEO} \cos(\delta) \sin(\alpha) \\ r_{GEO} \sin(\delta) \end{bmatrix} \quad (14)$$

where r_{GEO} is the geostationary orbit semi major axis and (α, δ) denote the geocentric right ascension and declination of the object. In addition, the observer's slant range vector $\vec{\rho}$ is resolved into components expressed in the topocentric (observer's) coordinate frame as Eq. (15). The topocentric right ascension and declination are denoted with subscripts "t", such as α_t, δ_t , to differentiate them from geocentric coordinates (α, δ)

$$\vec{\rho} = \begin{bmatrix} \rho_x \\ \rho_y \\ \rho_z \end{bmatrix} = \begin{bmatrix} \rho \cos(\delta_t) \cos(\alpha_t) \\ \rho \cos(\delta_t) \sin(\alpha_t) \\ \rho \sin(\delta_t) \end{bmatrix}$$

$$\|\vec{\rho}\| = \sqrt{\rho_x^2 + \rho_y^2 + \rho_z^2} \quad (15)$$

The definition of right ascension and declination adheres to the convention used by the astrodynamics and astronomical community equations as follows:

$$\alpha_t = \tan^{-1} \left(\frac{\rho_y}{\rho_x} \right) \quad (16)$$

$$\delta_t = \sin^{-1} \left(\frac{\rho_z}{\|\vec{\rho}\|} \right) \quad (17)$$

An observation vector \mathbf{y} is formed by transforming the speckle measurements (ρ, θ) into differential right ascension and declination measurements $(\Delta \alpha_t, \Delta \delta_t)$.

Differential right ascension measurements derived from a speckle image require division by the object's topocentric declination to correctly scale the longitude for proper astrometry.

$$\mathbf{y}_i = \begin{bmatrix} \Delta \alpha_t \\ \Delta \delta_t \end{bmatrix}_i = \begin{bmatrix} \frac{\rho \sin(\theta)}{\cos(\delta_t)} \\ \rho \cos(\theta) \end{bmatrix}_i \quad (18)$$

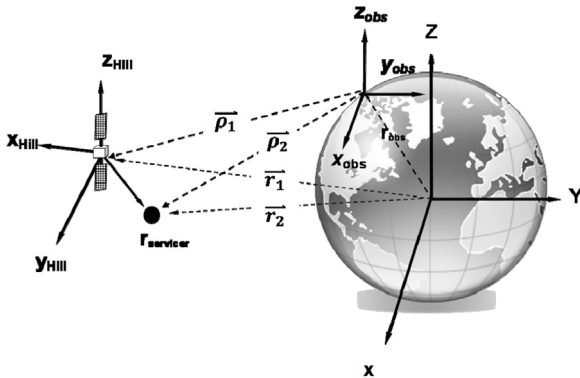


Fig. 5. Geometry of client and servicer observations.

The differential angular measurements of $(\Delta\alpha_t, \Delta\delta_t)$ describe the angular motion of the servicing satellite relative to the client. A transformation from geocentric coordinates to Hill coordinates is required. This is achieved by using a series of transformations. By taking the differentials of Eqs. (16) and (17), the differential right ascension and declination can be found (Eq. (19)) as a function of the differential position vector

$$\begin{bmatrix} \Delta\alpha_t \\ \Delta\delta_t \end{bmatrix} = \frac{1}{\|\mathbf{r}\|^2} \begin{bmatrix} -\rho_y & \rho_x & 0 \\ \frac{-\rho_x\rho_z}{(\rho_x^2 + \rho_y^2)} & \frac{-\rho_y\rho_z}{(\rho_x^2 + \rho_y^2)} & 1 \end{bmatrix} \begin{bmatrix} d\rho_x \\ d\rho_y \\ d\rho_z \end{bmatrix} \quad (19)$$

$$\Delta\vec{\mathbf{r}} = [d\rho_x \quad d\rho_y \quad d\rho_z]^T$$

where the vector $\Delta\vec{\mathbf{r}} = [d\rho_x \quad d\rho_y \quad d\rho_z]^T$ is expressed in the TOD coordinate frame and is the position vector of the servicing satellite relative to the client in this frame. This vector can then be rotated into the Hill coordinate frame by using the intermediate radial, tangential, orbit normal [RSW] [19] frame by forming a transformation matrix constructed of direction cosines

$$[R \mid S \mid W] = \begin{bmatrix} \frac{\mathbf{r}}{|\mathbf{r}|} & \frac{\mathbf{w} \times \mathbf{r}}{|\mathbf{w} \times \mathbf{r}|} & \frac{\mathbf{r} \times \mathbf{v}}{|\mathbf{r} \times \mathbf{v}|} \end{bmatrix} \quad (20)$$

where \mathbf{r} and \mathbf{v} are the inertial position and velocity vector of the primary object. As the Hill frame is a rotating coordinate frame it is important to compensate for Coriolis motion. This is achieved by compensating the angular velocity of the rotating frame relative to the RSW coordinate frame

$$\vec{\mathbf{v}}_{RSW} = \vec{\mathbf{v}}_{Hill} + \vec{\boldsymbol{\omega}}_{RSW} \times \vec{\mathbf{r}}_{Hill} \quad (21)$$

A compact version transforming the differential position vector to the Hill frame is expressed as

$$\begin{bmatrix} \Delta\vec{\mathbf{r}} \\ \Delta\vec{\mathbf{v}} \end{bmatrix} = [R \quad S \quad W] \begin{bmatrix} \mathbf{I}_{3 \times 3} & \mathbf{0}_{3 \times 3} \\ [\boldsymbol{\omega}_x] & \mathbf{I}_{3 \times 3} \end{bmatrix} \begin{bmatrix} \vec{\mathbf{r}}_{Hill} \\ \vec{\mathbf{v}}_{Hill} \end{bmatrix} \quad (22)$$

\mathbf{I} is a 3×3 identity matrix and the cross product is expressed as the skew symmetric matrix $\boldsymbol{\omega}_x$

$$\boldsymbol{\omega}_x = \begin{pmatrix} 0 & -\omega_z & \omega_y \\ \omega_z & 0 & -\omega_x \\ -\omega_y & \omega_x & 0 \end{pmatrix} \quad (23)$$

The differential angular measurements $(\Delta\alpha_t, \Delta\delta_t)$ can be now be directly expressed by combining Eqs. (19) (through 23) and converting the position vectors to their respective geocentric and topocentric angular equivalents by use of

$$\begin{bmatrix} \Delta\alpha_t \\ \Delta\delta_t \end{bmatrix} = \frac{1}{\rho_t} \begin{bmatrix} \frac{\sin(\alpha - \alpha_t)}{\cos(\delta_t)} & \frac{\cos(\alpha - \alpha_t)}{\cos(\delta_t)\cos(\alpha_t)} & 0 & 0 & 0 & 0 \\ -\cos(\alpha - \alpha_t)\sin(\delta_t) & \sin(\alpha - \alpha_t)\sin(\delta_t) & \cos(\delta_t) & 0 & 0 & 0 \end{bmatrix} \begin{bmatrix} \vec{\mathbf{r}}_{Hill} \\ \vec{\mathbf{v}}_{Hill} \end{bmatrix} \quad (24)$$

where the measurement matrix is expressed as:

$$\mathbf{H} = \frac{1}{\rho_t} \begin{bmatrix} \frac{\sin(\alpha - \alpha_t)}{\cos(\delta_t)} & \frac{\cos(\alpha - \alpha_t)}{\cos(\delta_t)\cos(\alpha_t)} & 0 & 0 & 0 & 0 \\ -\cos(\alpha - \alpha_t)\sin(\delta_t) & \sin(\alpha - \alpha_t)\sin(\delta_t) & \cos(\delta_t) & 0 & 0 & 0 \end{bmatrix} \quad (25)$$

The matrix \mathbf{H} expresses the transformation from the state variables expressed in Hill coordinates $\mathbf{X}_{Hill} = [x_{Hill}, y_{Hill}, z_{Hill}, v_{xHill}, v_{yHill}, v_{zHill}]^T$ to the differential angular measurements $\mathbf{y} = (\Delta\alpha_t, \Delta\delta_t)^T$ obtained by the sensor.

By incorporating the dynamics of the servicer's relative motion expressed in Eqs. (9)–(12) with the measurement matrix above, an Extended Kalman filter (EKF) implementation can be used to estimate the position and velocity of the servicing satellite in the Hill frame.

$$\text{Predicted covariance: } \bar{\mathbf{P}}_{k+1} = \boldsymbol{\Phi}\mathbf{P}_k\boldsymbol{\Phi}^T + \mathbf{Q} \quad (26)$$

$$\text{Predicted state: } \bar{\mathbf{x}}_{k+1} = \boldsymbol{\Phi}_{k+1,k}\hat{\mathbf{x}}_k \quad (27)$$

$$\text{Kalman Gain: } \mathbf{K}_k = \bar{\mathbf{P}}_k\mathbf{H}^T \left(\mathbf{H}\bar{\mathbf{P}}_k\mathbf{H}^T + \mathbf{R} \right) \quad (28)$$

\mathbf{P} , \mathbf{Q} , $\boldsymbol{\Phi}$, and k represent the a-priori covariance, process noise, state transition matrix and time step respectively. \mathbf{R} is the variance of the sensor measurement noise and \mathbf{K}_k is the Kalman gain. Using these expressions, the filtered, (updated) state $\hat{\mathbf{x}}_{k+1}$ (at time $k+1$) and covariance \mathbf{P}_{k+1} are shown in the following equation:

$$\text{Updated covariance: } \widehat{\mathbf{P}}_{k+1} = (\mathbf{I} - \mathbf{K}_k\mathbf{H})\bar{\mathbf{P}}_k \quad (29)$$

$$\text{Updated state: } \widehat{\mathbf{x}}_{k+1} = \bar{\mathbf{x}}_{k+1} + \mathbf{K}_k(\mathbf{y} - \mathbf{H}\bar{\mathbf{x}}_{k+1}) \quad (30)$$

6. Observability of relative motion

It should be understood that the \mathbf{H} matrix in Eq. (25) indicates that velocity is not a direct measureable from differential angular measures $(\Delta\alpha_t, \Delta\delta_t)$. The \mathbf{H} matrix has three columns of zeros due to the differential angular measurements being insensitive to the velocity of the object being measured.

The usual test for observability is to verify that the matrix $\mathbf{H}^T\mathbf{H} > 0$ is invertible and positive definite [19]. The presence of the zeroed columns in the right of Eq. (25) suggests that observability is an issue and resolving the radial offset between the satellites in the Hill frame is difficult to achieve.

7. Geostationary satellites as proxy observations of OOS motion

OOS servicing satellites are not currently employed in geostationary orbit therefore an observational proxy is required in order to test the cross spectrum observational approach. Many geostationary satellites are often co-located with other satellites within the same geostationary station-keeping box making it possible to test this estimation approach by observing an optical conjunction [10] of co-located geostationary satellites. The slight eccentricity and inclination offsets used by co-located geostationary satellites mimics a long-range formation flight case of OOS.

Typical co-location of geostationary satellites results in elliptical motion between 20 and 50 km.

Due to the brightness of the co-located cluster of Canadian satellites (Anik F1, Anik F1R and Anik G1 stationed at 107 °W) varying from 14th magnitude to 8th magnitude an application for observing time at the Observatoire Mont Mégantic [20] 1.6 m telescope (Fig. 6) was submitted. This telescope's high resolution and light gathering power (technical details in Table 1) increase the likelihood of detecting an optical conjunction during times that the satellites may be very faint due to the illumination and observation geometry. Optical conjunctions could occur at any time therefore an instrument with a large range of sensitivity helps increase flexibility to collect data.

A key technology used to exploit speckle data from the Mont Mégantic telescope is the use of a high frame rate 1024 × 1024 NuVu EM N2 liquid nitrogen cooled Electron Multiplied Charged Couple Device (EMCCD), [21] (see Table 2 and Fig. 7). These focal plane arrays use serial-register charge amplification in order to achieve exceptionally high signal to noise ratios making EMCCD an excellent choice for visible band speckle imaging of faint astronomical objects with short exposures. The EMCCD can acquire full frame speckle images from 16 to 20 Hz making it ideal for stacking speckle images of the optical conjunction and freezing the motion of the atmosphere.

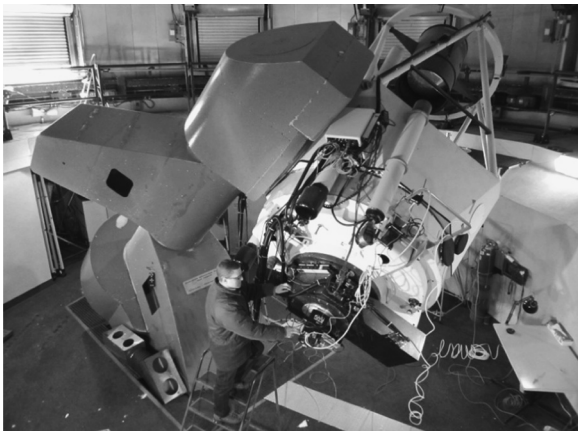


Fig. 6. The 1.6 m Mont Mégantic telescope.

Table 1
1.6 m telescope configuration.

Parameter	Range	units	Notes
Primary mirror diameter	1.55	m	
Secondary mirror diameter	0.57	m	
Observatory location			Geodetic coordinates
latitude	45.45519°	°N	
longitude	71.52734°	°W	
altitude	1059	m	
Focal length	12.8	m	
<i>f</i> / <i>#</i>	8	–	
Diffraction limit	5.4	μm	
Focal extension	8 × -102.4 m effective	m	2 × and 4 × parfocal barlows
EMCCD pixel scale	0.0251	″pix ⁻¹	
EMCCD field of view at 8 ×	26.8	arcsec	

The focal length of the 1.6 m telescope was increased using an arrangement of 2 × and 4 × parfocal barlow lenses to an effective focal length to 102.4 m. This was to ensure that the point spread function of the 1.6 m spanned at least 2 pixels of the EMCCD so that each speckle could be Nyquist sampled. This long focal length reduced the effective field of view of the EMCCD to a 27 arcsec square, adding considerable complexity to the process of finding and centering the satellites. Use of a separate low light video camera and guide telescope helped re-center the satellites in the EMCCD field of view.

7.1. Sensor calibration

Binary stars were used to calibrate and test the camera by validating the pixel scale and true north direction of the detector. A diffraction slit mask for the Mégantic telescope was not available therefore another means to validate the pixel scale of the detector was required. A widely spaced, high elevation double star pair was selected from the Washington Double Star Catalog [22], WDS 326BC (Fig. 8, left) and imagery was acquired both normally and speckle imaged. The pixel scale was validated by measuring the pixel centroid locations of the components of the binary star pair and by comparing the current separation of the binary (see Table 3) to the 1899 separation (ρ) measurements. As little relative motion of this binary has been observed it provided a means to validate the angular pixel scale for the detector which was found to be 0.0251 arcsec per pixel.

To confirm the north orientation of the instrument a long duration exposure of the EMCCD was taken and the sidereal drive of the 1.6 m telescope was abruptly turned off mid-exposure. The resulting star trails (Fig. 8 right) indicate the west direction on the detector and celestial north can be immediately reckoned to be 90° counter-clockwise relative to the star trails.

7.2. Observational findings

A optical conjunction (two satellites appearing to intersect each another with respect to an observer) between Anik G1 and Anik F1R was forecasted using a propagated ephemeris supplied by Telesat Canada. Prior to

Table 2
Nuvu EM N2 EMCCD properties.

Parameter	Range	units	Notes
Digitization	16	bit	
Pixel pitch	13	μm	
Array dimensions	1024 × 1024 (13.3 × 13.3)	Pixels (mm)	
Dark Current (N_{DC})	0.001	$e^- \text{pix}^{-1} \text{s}^{-1}$	@ -85 °C
Peak QE	90	%	@600 nm
Full frame rate	16	Hz	
EM gain range	1–5000	–	
Read noise	0.1	e^-	
Spectral range	250–1100	nm	
Read noise w/EM gain	< 3	e^-	@100 kHz
Read noise w/out EM gain	< 0.1	e^-	@20 MHz

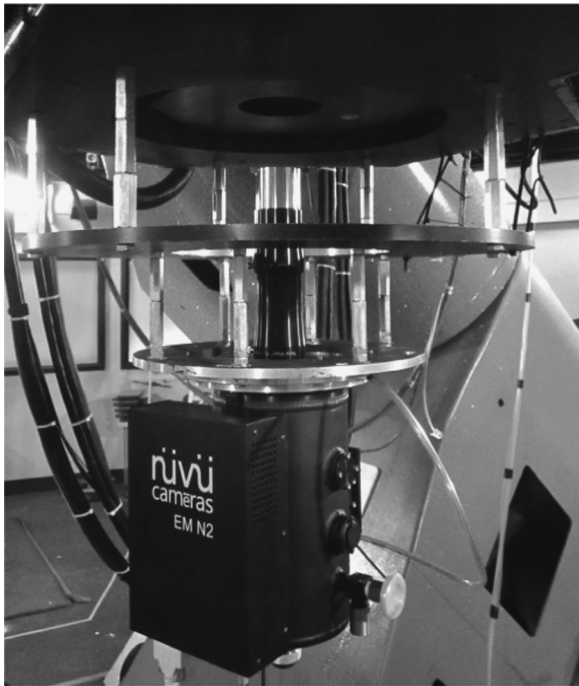


Fig. 7. Nuvu EMCCD and barlows fitted to the prime focus of the Mont Mégantic telescope.

data acquisition, Anik G1 was imaged individually to measure the atmospheric seeing by measuring the full width half maximum of the point spread function (spot size) on the detector plane. The seeing was measured to be 2.1 arcsec which is considered to be moderate seeing conditions.

A short period of time was required for both satellites to enter the narrow field of view of the EMCCD. Once both objects were on the detector, 10 ms exposures were acquired at a 20 Hz rate. Anik F1R traversed just slightly ahead and upward relative to Anik G1 (Fig. 9). A slight elongation of the object point spread functions was observed and is believed to be chromatic dispersion due to the relatively low elevation angle at which the two satellites were observed ($\sim 27^\circ$). Sample images collected at various times during the optical conjunction are shown in the top row of Fig. 10.

The telescope mount's sidereal tracking was turned off and non-sidereal rates were applied to compensate for the slight differential motion that the satellites have relative to the Earth. During acquisition the EMCCD collected 4910 full frame images over a 10 min timespan. A short pause in data collection just after the satellites' closest approach was needed to re-center the satellites in the field of view as the drift rate of the pair was not completely compensated by the non-sidereal mount rates.

8. Data processing

Automated data processing code was developed in Matlab. Stacks of 20 images which constitute approximately one second of time were batch processed after the data acquisition. The average of the start and finish time of the frame stacks was used as the time tag for the differential measurements. Processing time for the 10 min track of data required approximately 20 min on a modest Pentium computer².

During processing it was observed that large separation distances (~ 5 arcsec) resulted in the strongest cross spectrum fringes, making it easy for the algorithm to ascertain the orientation and separation between the two satellites. The orientation angle of the fringes was automatically detected via Radon transform detection of the fringe angles (refer to Fig. 10, lower row). While the Radon transform is effective at detecting strong lines in imagery it does incur periodic “stepping” of the fringe orientation angle due to the finite resolution of the transform's angle search space. This causes a noticeable “locking” of orientation angle from stack to stack until the satellites' motion transitions to the next integer pixel which transitions the Radon's best fit angle to the next value. This incurs processing error on the imagery of approximately 0.05 arcsec.

It was found that the imaginary component of the fringe data was quite reliable as an indicator of the orientation of the secondary satellite relative to the primary. This component is rather insensitive to image noise. However, during times when the separation between the two objects closed within 1 arcsec the imaginary

² The repetitive nature of stacking and averaging cross spectrum data lends itself well to parallelization for real-time data acquisition.

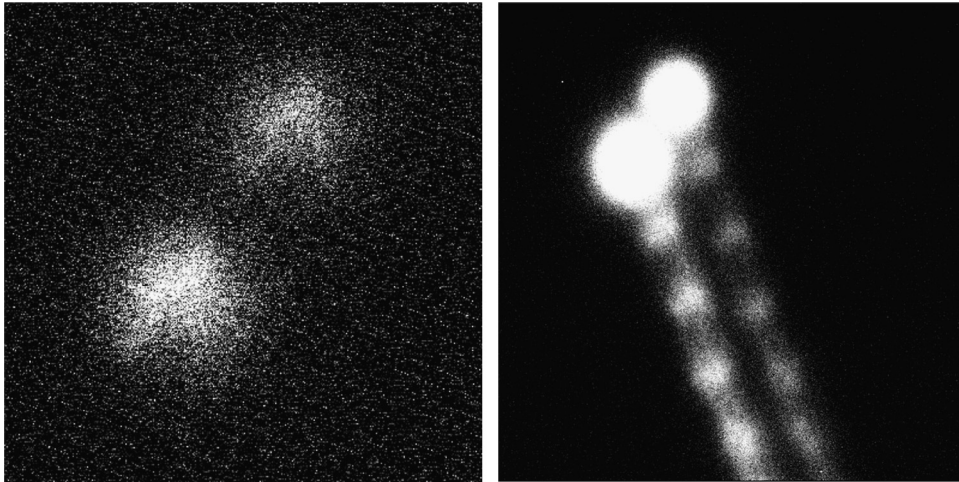


Fig. 8. Left: speckle image of WDS ES326BC. Right: trailing of stars to establish West orientation of detector.

Table 3
WDS ES326 BC data from reference [21].

Parameter			Units
WDS identifier	03058 + 3202ES326BC		
Year of measurement	1899	2010	
ρ	4.1	4.3	arcseconds
θ	34	34	degrees
Magnitudes	10.99 primary	12.0 secondary	Vmag

component of the cross spectrum became somewhat chaotic (Fig. 10, lower data set, center image). While the imaginary component works well in most cases more development is required for separation distances less than 1 arcsec.

9. Discussion of results

Fig. 10 shows the select history of the images and cross spectrum fringe measurements during the ten-minute data acquisition timespan. The measurements were reliably obtained until the satellites' separation became less than half of the point spread function size (~ 1 arcsec). At this time the imaginary component of the fringe data becomes degenerate and lacks the clean linear fringe shapes needed to determine the orientation and separation of the two satellites. Fig. 11 shows the ρ, θ measurement history inferred from the fringe data. When the separation distance became less than 1 arcsec, large θ ambiguity jumps of 180° were seen and resulted in erratic ρ measurements. The θ plot (Fig. 11 bottom) shows relatively smooth motion of Anik F1R relative to Anik G1 with the exception of the ambiguity phase and the reacquisition time period required in order to re-center the satellites in the middle of the field of view just after closest approach.

Fig. 12 shows a consistency plot between the measured $\Delta\alpha_t, \Delta\delta_t$ relative position against the reference ephemeris

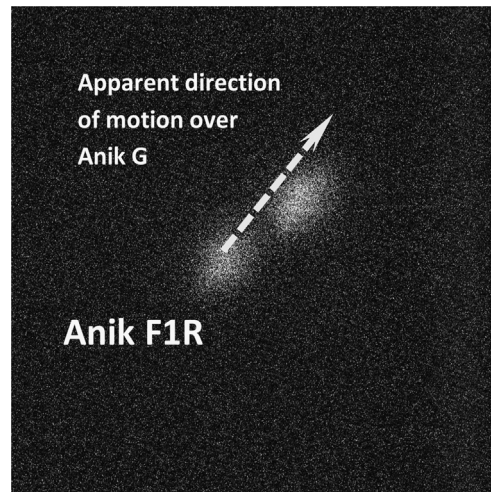


Fig. 9. Anik F1R (center) and Anik G1 (upper right) imaged with the EMCCD and the Mégantic 1.6 m.

for the two satellites. Very good consistency in $\Delta\alpha_t$ was observed and was less than 0.5 arcsec with a slight positive differential right ascension bias of ~ 0.3 arcsec. Measurements obtained in $\Delta\delta_t$ were less than 0.2 arcsec and tended to be biased by $+0.5$ arcsec higher than the ephemeris. These biases may be indicative of actual cross-track position differences between ephemeris and actual

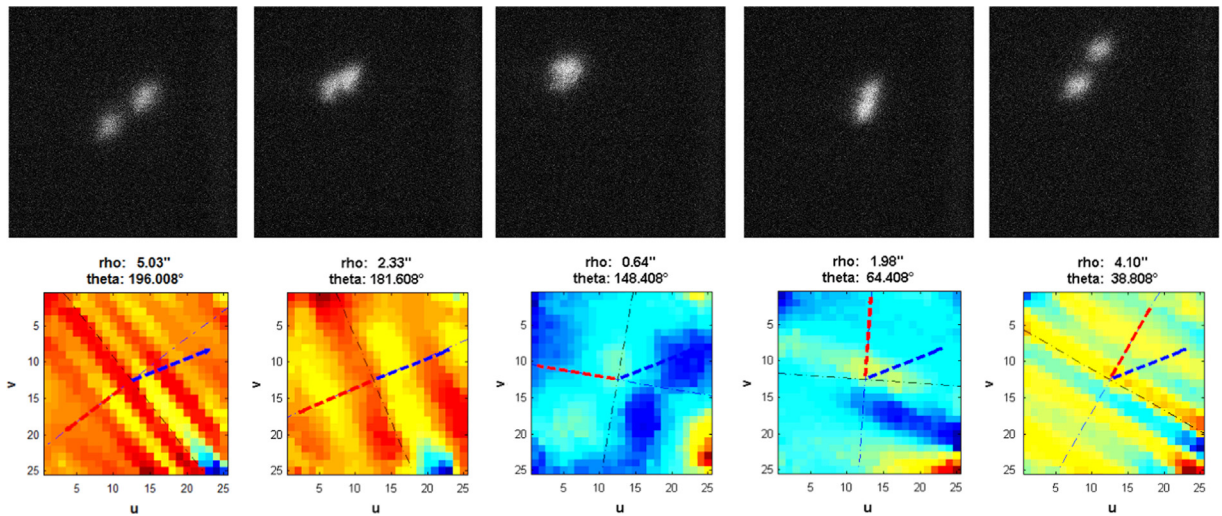


Fig. 10. Upper row: selected frames from the motion of Anik F1R relative to Anik G1. Lower row: Modulus of cross spectrum fringe measurements for 20 image stacks. The rotating dashed line indicates the direction of the fainter object (Anik F1R). The non-rotating dashed line is the direction to celestial north.

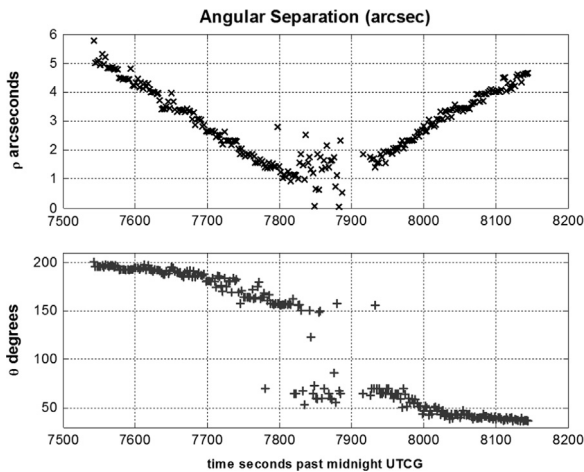


Fig. 11. (Upper) ρ separation distance (x) between the two satellites during the optical conjunction, (Lower): θ orientation angle (+) with respect to celestial north.

positions. Timing inaccuracy on the camera acquisition computer may be a possible source of this bias as a USNO server time server was used (a GPS time source was not available at the observatory). A 60-s offset, which can easily occur on many computer clocks, could explain the biases seen in Fig. 12. Alternatively, geostationary satellite ephemerides, while highly precise in radial positioning are known to experience in-track inaccuracies due to uncompensated range-bias during their ephemeris creation. It is difficult to ascertain from this single track if the bias is due to errors in sensor timing or satellite ephemeris.

9.1. Relative orbit estimation

An initial state vector was derived from the satellite ephemeris corresponding to an epoch of 18 Feb 2014 at 2^h05^m UTC. A large initial covariance of $P = \text{diag} [1^2, 1^2, 1^2, 0.001^2, 0.001^2, 0.001^2]$ (km², km²/s²) was used to set the

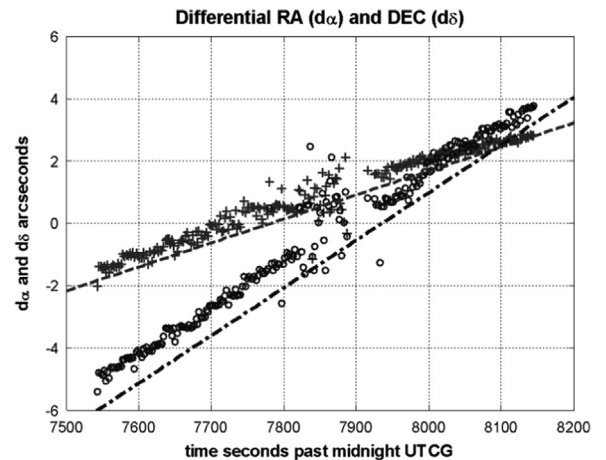


Fig. 12. Differential right ascension measurements $\Delta\alpha_t$ (+) plotted against reference ephemeris (dashed). Differential declination measurements $\Delta\delta_t$ (o) plotted against reference ephemeris (dashdot).

initial uncertainty of the system. A process noise estimate consisting of a diagonal matrix of small elements $Q = \text{diag} [0.5^2, 0.5^2, 0.5^2, 0.001^2, 0.001^2, 0.001^2]$ (m², m²/s²) was used during the execution of the filter.

Radial, in-track, and cross-track (RIC) position error compared to the ephemeris position of Anik F1R is shown in Fig. 13. Anik G1's ephemeris was used as the reference frame for both reference ephemeris and filtered satellite position. Overall consistency was less than 1.8 km and showed excellent consistency with Anik F1R's reference to less than 0.1 km until mid-track. During the ambiguity phase the EKF appears to have accepted bogus positional measurements which resulted in the relative orbit diverging past 2:11 UT. A visualization of the measured relative orbit is shown in Fig. 14 which initially shows good consistency with the reference position, however radial error builds during the ambiguity phase resulting with a

+1.8 km radial position offset. As measurements continued to be collected it suggests that the EKF is not handling bad measurement data properly.

The 1-sigma relative position covariance information is shown in Fig. 15. The radial position error (sigma x) is the largest uncertainty in the track manifesting as a 1–1.1 km overall error. The in-track (sigma y) and cross-track (sigma z) errors are within 0.04 and 0.11 km respectively. The error growth rate in the radial direction is of particular concern as continued observations did not result in a better estimated relative orbit during the ten minute tracking interval.

In order to understand the growth in the radial component of the positional covariance a simulation of the differential measurement data was performed over an extended virtual tracking period up to 12 h duration mimicking a full night's tracking on the orbital position of Anik F1R. It was found that the error growth rate in all axes was arrested after 0.5 h of tracking and converged after 6 h (Fig. 16). This suggests a necessity for prolonged tracking periods of several hours in order to properly

estimate the radial offset between the client and servicing satellite. These results also suggest a more careful examination of the dynamics and process noise model is required. This work will be performed in the future.

10. Conclusion

Cross spectrum analysis of speckle imaging shows promise for relative orbit estimation of closely separated objects in geostationary orbit. Experimental measurements obtained over a 10 min tracking interval on co-located satellites generated filtered relative orbit position errors consistent with the sensor noise in the in-track and cross-track directions on satellites with separations from 5 to 1 arcsec. The tracking interval was too short to fully estimate the radial position and error growth in this axis was observed. Simulations indicate that relative orbit convergence is achieved after 4 h of tracking data revealing that larger arcs of data must be collected to enable relative orbit estimation. While refinement is necessary,

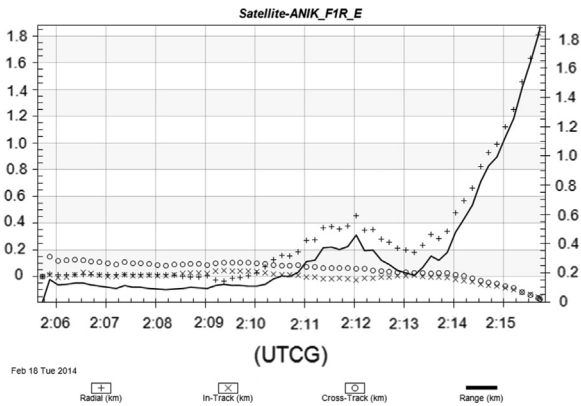


Fig. 13. Radial, in-track and cross track (RIC) position differences from the filtered observations compared to ephemeris.

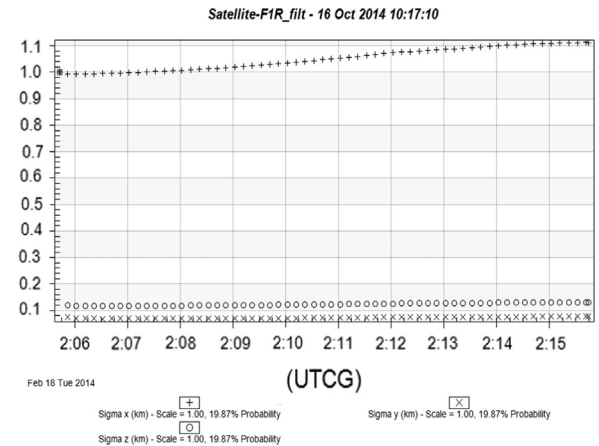


Fig. 15. (1σ) Filtered Anik F1R position covariance.

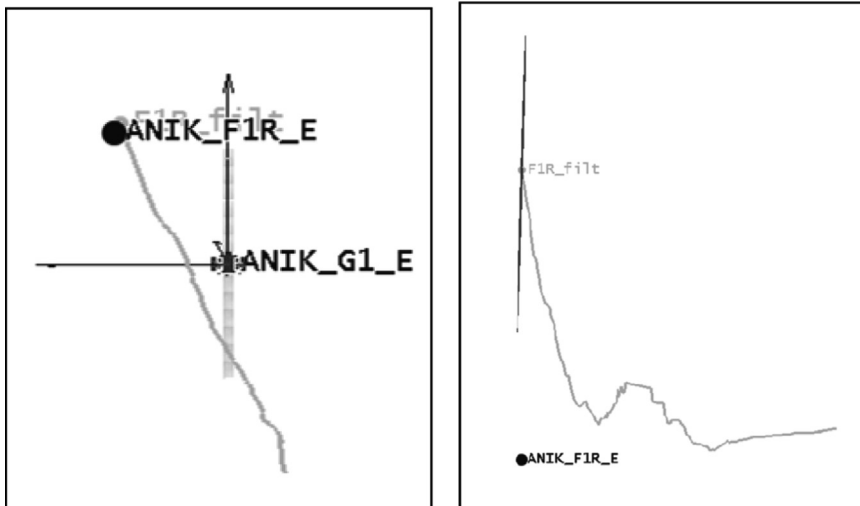


Fig. 14. Left: cross-track and in-track position of Anik F1R showing good relative position consistency with Anik F1R's reference ephemeris. Right: radial and in-track position showing the radial error growth (initial path of motion is from right to left).

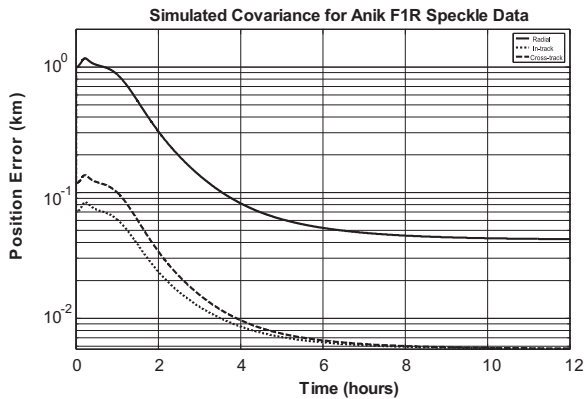


Fig. 16. (1σ) Simulated position covariance.

this approach offers a potential path for the space surveillance of complex, future on-orbit servicing missions in geostationary orbit.

Acknowledgments

The authors wish to acknowledge the tremendous support of many personnel and organizations that helped enable this work. Acknowledgment is extended to Defence R&D Canada Ottawa Research Centre for its direct support of this work (project 05BA); the Department of National Defence's Director General Space (DGSpace), the Department of Mechanical and Aerospace Engineering at Carleton University, Ottawa, Canada and Tim Douglas at Telesat Canada.

This work would not have been possible without the observing time granted by Robert Lamontange (University of Montreal) and technical support from the high caliber observatory staff of the 1.6 m telescope at Observatoire du Mont-Mégantic, in Mont-Mégantic, Quebec. The author was also exceptionally fortunate to have access to one of the highest performance EMCCDs available and appreciation to Oliver Daigle, Felecien Legrand and Phillippe Richelet at Nuvu Camera Inc. is extended.

References

- [1] National Aeronautics and Space Administration Space Shuttle Mission STS-41C Press Kit, NASA release No 84-38, March. (http://www.jsc.nasa.gov/history/shuttle_pk/pk/Flight_011_STS-41C_Press_Kit.pdf), 1984 (accessed 28.08.14).
- [2] STS-88 ISS construction mission, (<http://science.ksc.nasa.gov/shuttle/missions/sts-88/mission-sts-88.html>) (accessed 27.08.14).
- [3] Engineering Test Satellite VII (ETS-VII). (http://robotics.jaxa.jp/project/ets7-HP/ets7_e/rvd/rvd_index_e.html#FP-1) (accessed June 2009).
- [4] R. Madison, Micro-satellite based, on-orbit servicing work at the air force research laboratory, in: Proceedings of the IEEE Aerospace Conference, 2000, pp. 215–226.
- [5] Robotic Refueling Mission, NASA facts, Satellite Servicing Capabilities office. (http://ssco.gsfc.nasa.gov/images/RRM_2013_Factsheet_07.pdf) (accessed July 2014).

- [6] T. Mulder, Orbital Express Autonomous Rendezvous and Capture Flight Operations, part 1 of 2: Mission Description, AR&C Exercises 1,2,3, AAS Spaceflight Mechanics Meeting, 2008, Galveston TX.
- [7] Intelsat Picks MacDonald Dettwiler and Associates Ltd for Satellite Servicing, 15 March 2011. (<http://www.newswire.ca/en/story/730363/intelsat-picks-macdonald-dettwiler-and-associates-ltd-for-satellite-servicing>) (accessed July 2014).
- [8] Vivisat web site. (<http://www.vivisat.com/>) (accessed July 2014).
- [9] DARPA Phoenix website. (http://www.darpa.mil/Our_Work/TTO/Programs/Phoenix.aspx) (accessed July 2014).
- [10] R.L. Scott, B. Wallace, Small Aperture Telescope Observations of Co-located geostationary satellites, in: Proceedings of the AMOS Technical Conference, Maui HI, 2009.
- [11] S. Kawase, Real time relative motion monitoring for co-located geostationary satellites, J. Commun. Res. Lab. 36 (148) (1989) 125–135. (Tokyo, Japan).
- [12] S. Kawase, Differential Angle Tracking for Close Geostationary Satellite, J. Guid Control Dyn. 16 (6) (1993) 1055–1060.
- [13] K. Knox, Observations of the 2012 near occultation of planet Pluto, in: Proceedings of the AMOS Technical Conference, Maui HI, 2009.
- [14] A. Labeyrie, Attainment of diffraction limited resolution in large telescopes by Fourier analyzing speckle patterns in star image, Astron. Astrophys. 6 (1970) 85–87.
- [15] W.G. Bagnuolo, B. Mason, D.J. Barry, Absolute quadrant determinations from speckle observations of binary stars, Astron. J. 103 (4) (1992) 1399–1407.
- [16] E. Aristidi, M. Carillet, J-F Lyon, C. Aime, Imaging binary stars by the cross-correlation technique, Astron. Astrophys. Suppl. Ser. 125 (1997) 139–148.
- [17] W.H. Clohessy, R.S. Wiltshire, Terminal guidance system for satellite rendezvous, J. Aerosp. Sci. 27 (9) (1960) 653–658.
- [18] G. Hill, Researches in Lunar Theory, Am. J. Math. 1 (1878) 5–26.
- [19] D.A. Vallado, Fundamentals of Astrodynamics and Applications, 4th ed. Microcosm, Hawthorne, CA, 2013.
- [20] Observatoire Mont Mégantic. (<http://omm.cra-qastro.ca/>) (accessed January 2014).
- [21] O. Daigle, CCCP, A CCD Controller for Counting Photons, SPIE 13, 7014 Ground Based and Airborne Instrumentation for Astronomy II, (http://www.astro.umontreal.ca/~odaigle/spie_13_2008.pdf), 2008.
- [22] Washington Double Star Catalog, United States Naval Observatory, accessible via. (<http://ad.usno.navy.mil/wds/>) (accessed Feb 2014).



Robert (Lauchie) Scott, P.Eng, is a Defence Scientist at Defence R&D Canada's Ottawa Research Center. He conducts optical space situational awareness research for both ground and space based tracking platforms. Mr. Scott is a mission scientist for the High Earth Orbit Space Surveillance (HEOSS) portion of the NEOSat microsatellite technology demonstration project and he was the project manager of the Surveillance of Space Ground Based Optical system. He has a bachelor's degree in mechanical engineering from the Technical University of Nova Scotia and a

master's degree in space sciences from the Florida Institute of Technology. Mr. Scott is a Ph.D. candidate in aerospace engineering at Carleton University.



Dr. Alex Ellery is a professor of Mechanical and Aerospace Engineering at Carleton University. Dr Ellery is the Canadian research chair in space, robotics and space technology. His research interests include space robotics, space exploration, on-orbit servicing, planetary rovers, micro rovers, self-replicating robotics and in-situ resources extraction from asteroids or other solar system bodies. He has a bachelor's of science from Ulster, M.Sc., from Sussex, and a Ph.D. from University of Cranfield (United Kingdom).